





Self-pulsing dynamics in microscopic lasers with dispersive mirrors

Kristian Seegert ^{*}, Mikkel Heuck , Yi Yu , and Jesper Mørk 

Department of Electrical and Photonics Engineering, Technical University of Denmark, Building 345, 2800 Kgs. Lyngby, Denmark and NanoPhoton - Center for Nanophotonics, Ørsted's Plads 345A, 2800 Kgs. Lyngby, Denmark



(Received 6 February 2024; accepted 14 May 2024; published 13 June 2024)

We show that a passive dispersive reflector integrated into a semiconductor laser can be used to tailor the laser dynamics for the generation of ultrashort pulses as well as stable dual-mode lasing. We analyze the stability using a general model that applies to any laser with frequency-dependent mirror losses. Finally, we present a generalization of the Fano laser concept, which provides a flexible platform for tailoring the mirror dispersion for self-pulsing. In addition to functioning as a design guideline, our model also accounts for several results in the literature.

DOI: [10.1103/PhysRevA.109.063512](https://doi.org/10.1103/PhysRevA.109.063512)

I. INTRODUCTION

The generation of optical pulses plays a crucial role in many photonic technologies, including communications [1], spectroscopy [2], all-optical clock recovery [3], sensing [4], and LiDAR. In addition, excitable spiking nanolasers may act as “photonic neurons” in neuromorphic computing [5,6]. Much effort has been put into reducing the size and increasing the energy efficiency of pulsed lasers [7]. However, passive Q -switching in a microscopic laser was only demonstrated recently [8,9]. All current demonstrations of Q -switched nanolasers rely on the presence of an element in the laser cavity that exhibits saturable absorption, such that the laser favors operation in a pulsed rather than a continuous wave state. Saturable absorbers require control of the carrier lifetimes, which need to be shorter in the absorber section than in the gain section [10]. This is done by using different materials, by reverse biasing the absorber section, or by modifying the lifetimes in other ways, e.g., passivating the active section.

An alternative way of generating self-pulsing relies on passive dispersive reflectors (PDRs) [11–16]. Compared to saturable absorbers, PDRs may allow a lower lasing threshold (there are no losses that first need to be saturated) and engineered output pulses. Another advantage of PDRs is that they are material independent, relying only on the geometry of the design.

So far, modeling of lasers with dispersive mirrors has mainly been done by implementation-specific approaches, and this prevents general conclusions from being drawn about their possibilities and limitations. Here, we provide a unified description of how a dispersive mirror influences the dynamical properties of the laser and, in particular, its stability. For microscopic lasers, referring only to the local slope and curvature of the mirror reflection spectrum, we are able to predict the onset of self-pulsing.

We keep the details of the PDR general and instead focus on the inverse problem: what kinds of dynamic instabilities can arise, and how does the onset of instabilities relate to the PDR reflection spectrum? We show that a generalization of the Fano laser [17,18] provides a flexible platform for tailoring the mirror response. In particular, we demonstrate the possibility of generating short optical pulses (see Sec. III), as well as stable dual-mode lasing corresponding to beating oscillations (see Sec. IV) with a tunable beat-note frequency much smaller than the free spectral range of the cavity. As a key result, we derive a modified characteristic equation for the linearized system that explicitly takes into account the frequency-dependent mirror response. We derive a general expression for the relaxation oscillation frequency and damping rate that depends on the local shape of the reflectivity $r_R(\omega)$. This expression may be applied as a guideline for the design of the PDR. Furthermore, it provides a simple and general explanation of various results already presented in the literature regarding the impact of a frequency-dependent mirror on relaxation oscillations.

The coupled-cavity Fano laser

Our proposed generalization of the Fano laser is illustrated schematically in Fig. 1(a). It consists of a semi-open waveguide that is side-coupled to two nanocavities. The left mirror is broadband and formed by terminating the waveguide, while the right mirror is based on Fano interference between the nanocavities and the waveguide, making its reflectivity, $r_R(\omega) = |r_R(\omega)| \exp[i\phi(\omega)]$, strongly frequency dependent [19]. Importantly, a buried heterostructure [20,21] ensures that gain material only exists in the waveguide segment between the left mirror and the leftmost nanocavity. The nanocavities are thereby completely passive, with $r_R(\omega)$ being independent of the carrier density N .

The original Fano laser is based on a single side-coupled nanocavity [17,18]. In the case of a single nanocavity, the transmission in the waveguide below the nanocavity will have two contributions corresponding to two different optical

^{*}Contact author: krsee@dtu.dk

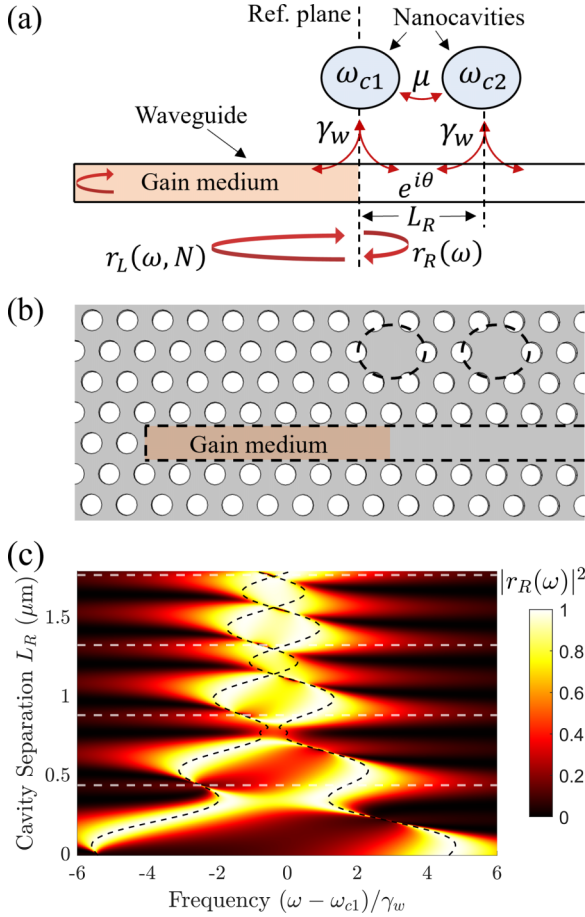


FIG. 1. (a) Schematic of the coupled-cavity Fano laser. Reflection off of the left mirror and propagation through the active region with carrier density N is described by $r_L(\omega, N)$. The reflection from the two coupled cavities on the right is $r_R(\omega)$. The cavities are sketched as the two ellipses labeled with their bare resonance frequencies at ω_{c1} and ω_{c2} . They are evanescently coupled with a rate μ and indirectly through a waveguide of length L_R and propagation constant k . (b) Sketch of a possible realization of the coupled-cavity Fano laser in a 2D photonic crystal membrane. (c) 2D reflectivity map of $|r_R(\omega)|^2$ (color scale) vs frequency ω and cavity separation L_R . The coupling phase is $\theta = kL_R$, and the evanescent coupling between the cavities is modeled as $\mu = 5\gamma_w \exp(-L_R/\kappa)$, where $\kappa = 0.5\mu\text{m}$. The white dashed lines denote where $\theta = 0 \bmod 2\pi$. The detuning between the cavities is set to $\Delta = -0.78\gamma_w$ ($\Delta/2\pi = -100$ GHz), and the Q factor related to coupling to the waveguide is set to $Q_w = 750$ for both cavities. The intrinsic quality factor is set to $Q_i = 10^5$.

pathways, namely, direct propagation in the waveguide, and coupling to the nanocavity and back into the waveguide in the same direction. If the frequency of the incoming wave matches the resonance frequency of the nanocavity, destructive interference occurs between these two optical pathways, and the result is a narrow-band mirror with a Lorentzian reflection spectrum [22]. The conventional Fano laser has already shown many interesting properties and dynamics, including the theoretical possibility of terahertz frequency modulation [17], stability toward coherence collapse [23], self-pulsing (in the case where the active material extends into the nanocavity

[8]), ultra-narrow linewidth (in the case where the active material is confined to the waveguide section similar to Fig. 1) [21], and the possibility to dynamically modulate the mirror losses [24]. In addition to functioning as narrow-band mirrors, Fano resonances also have interesting possible applications in all-optical switching, signal processing, and frequency conversion [25].

In the present case, the addition of a second nanocavity to the original Fano laser [17] allows additional possibilities for engineering the mirror reflectivity, which can be analyzed by temporal coupled-mode theory [26]. Note that in addition to being placed on the same side of the waveguide as depicted in Fig. 1(a), the cavities can also be placed on opposite sides as in Refs. [27,28]. The spectral response of the dispersive reflector is determined by the cavity detuning $\Delta = \omega_{c2} - \omega_{c1}$, the evanescent coupling rate μ , and the indirect waveguide coupling described by the propagation phase $\theta = kL_R$, see Fig. 1(a).

We note that the Fano laser concept is agnostic to the details of how the waveguide and the cavities are formed, but one possible implementation is in a two-dimensional (2D) photonic crystal membrane as sketched in Fig. 1(b). In this case, confinement in the out-of-plane direction is due to total internal reflection, while confinement in-plane is due to the photonic band gap [29]. A line-defect waveguide can then be formed by removing a row of holes, while point-defect cavities can be formed by removing a limited number of holes, here shown as one. Alternatively, one-dimensional (1D) photonic crystal nanobeams can be used for both the waveguide and the side-coupled cavities, as recently demonstrated for the single-cavity Fano laser in Ref. [30].

Figure 1(c) shows a 2D map of the reflectivity $|r_R(\omega)|^2$ versus frequency and nanocavity separation L_R for a detuning of $\Delta/2\pi = -100$ GHz. In order to represent the dependence on both the evanescent and indirect coupling in a straightforward manner and illustrate some general tendencies, we use a simple model where the evanescent coupling falls off as $\mu = \mu_0 \exp(-L_R/\kappa)$, where κ is some characteristic length. The white dashed lines show where $\theta = 2\pi m$. Note, in the specific case of a 2D photonic crystal the exponential dependence is not exactly valid [31].

We can understand the reflectivity spectrum in Fig. 1(c) as follows: The two cavities form two supermodes with complex frequencies $\tilde{\omega}_{\pm} = \omega_{\pm} - i\gamma_{\pm}$ which are hybridizations of the modes of the uncoupled cavities, and each supermode will be accompanied by a Lorentzian frequency dependence of the reflectivity,

$$r_R(\omega) = \frac{d_+^2}{i(\omega_+ - \omega) + \gamma_+} + \frac{d_-^2}{i(\omega_- - \omega) + \gamma_-}, \quad (1)$$

where the complex coupling coefficients d_{\pm} are given in Appendix A. The real part of the resonance frequencies are shown as the black dashed lines. In our case, the complex supermode frequencies are given by

$$\tilde{\omega}_{\pm} = \frac{\omega_{c1} + \omega_{c2}}{2} - i(\gamma_w + \gamma_i) \pm \sqrt{\left(\frac{\Delta}{2}\right)^2 + (\mu + i\gamma_w e^{i\phi_w})^2}, \quad (2)$$

where γ_w is the coupling rate between the nanocavities and the waveguide, and γ_i represents intrinsic losses, both of which are assumed to be identical for the two cavities. The total coupling phase, $\phi_w = \phi_{1R} + \theta + \phi_{2L}$, includes the propagation phase θ and the coupling phases ϕ_{1R} and ϕ_{2L} associated with coupling from cavity 1 to the right and cavity 2 to the left, respectively. Further, if the cavities are identical, then the relation $\exp(i\phi_{1R} + i\phi_{2L}) = -1$ can be derived from coupled-mode theory [22].

When the nanocavity separation L_R is small, such that the evanescent coupling is strong ($\mu \gg \gamma_w$), the resonances are clearly split, but they start to overlap as the cavities get further apart. The reflection occurs via different optical paths, and interference between them causes variations in the positions and widths of the Lorentzian resonances.

If the cavities are identical, the supermodes will be equal-amplitude superpositions of the individual cavity modes. We will refer to $\tilde{\omega}_+$ ($\tilde{\omega}_-$) as the ‘‘bonding’’ (‘‘antibonding’’) mode corresponding to the cavity fields being phase-shifted by 0 (π). For $e^{i\theta}$ approaching 1, the outgoing waves of each cavity interfere constructively (destructively) for the bonding (antibonding) supermode, leading to broadening (narrowing) of the associated resonance peak, making the spectrum highly asymmetric. This phenomenon of loss-splitting is referred to as *dissipative coupling*, and exactly when $e^{i\theta} = 1$ [white dashed lines in Fig. 1(c)], we get an example of a bound state in the continuum (BIC), which does not couple to the waveguide at all [32]. In other words, if the leaky cavity modes have the same far-field radiation pattern, then the out-of-phase (antibonding) supermode will cancel out in the far field, leading to a high Q factor. The same effect takes place for $e^{i\theta} = -1$, but with the broadening and narrowing being reversed. On the other hand, when $e^{i\theta} = \pm i$, the outgoing waves are phase shifted by $\pi/2$, which only affects the real part of the resonance frequencies, resulting in a symmetric spectrum. This case, where $\text{Im}(\mu + i\gamma_w e^{i\phi_w}) = 0$, is referred to as *dispersive coupling*.

While coupled mode theory has been shown to accurately account for the dispersive properties of systems composed of coupled waveguides and cavities [33], actual designs will, of course, need to rely on numerical calculations, using, e.g., finite-difference time-domain (FDTD) or finite-element calculations.

Using dual-cavity reflectors, several works illustrate the large freedom one has to engineer the spectral shape of the reflection spectrum by modifying the geometry of the cavities, including their relative positions [31], the potential barrier between the cavities [34], and possibly adding blocking elements in the waveguide [27]. Finally, in addition to tuning the response through the designed geometry, it is also possible to dynamically modulate the cavities through nonlinear effects [24,35], or by electrodes that change the refractive index of the nanocavity through an applied electrical field.

The ability to manipulate the mirror’s response opens up avenues to design laser dynamics, as the wide range of reflection spectra may lead to very different dynamical regimes. Next, we turn to the question of how a frequency-dependent mirror affects the laser dynamics. After the general analysis, we provide two examples of applications: self- Q -switching and dual-mode lasing.

II. GENERAL STABILITY ANALYSIS

A. Modal properties of lasers with dispersive mirrors

The general analysis in this section applies to any laser that can be modeled as an effective Fabry-Perot laser with a dispersive mirror. In order to get a better understanding of the dynamics of lasers with dispersive mirrors, we will introduce the concepts of *steady-state modes*, *antimodes*, *instantaneous modes*, and *sidemodes*. Additionally, steady-state modes and antimodes are referred to collectively as *steady-state solutions*.

We define the forward- and backward-propagating complex electric fields at a reference plane just left of the PDR [see Fig. 1(a)] as $E(\omega)$ and $E_-(\omega)$. They are related by [36]

$$E(\omega) = r_L(\omega, N)E_-(\omega) + F(\omega), \quad (3)$$

$$E_-(\omega) = r_R(\omega)E(\omega), \quad (4)$$

where $F(\omega)$ is a term representing spontaneous emission and noise. The function $r_L(\omega, N)$, which represents a round trip in the active section with carrier density N , is given by

$$r_L(\omega, N) = r_1 e^{2ik(\omega, N)L}, \quad (5)$$

where r_1 is the reflectivity of the frequency-independent left mirror, $k(\omega, N)$ is the wave number, and L is the length of the active section.

We define the *instantaneous modes* $\tilde{\omega}_n(N)$ as the complex solutions to the oscillation condition

$$r_L(\tilde{\omega}_n, N)r_R(\tilde{\omega}_n) = 1, \quad \tilde{\omega}_n \in \mathbb{C}, \quad (6)$$

where the carrier density is interpreted as a parameter. The instantaneous modes trace out branches of solutions in the complex frequency plane that depend parametrically on N , and the subscript ‘‘ n ’’ denotes a particular solution branch. For a frequency-independent right mirror, the different branches of instantaneous modes would correspond to different Fabry-Perot longitudinal modes, where the round-trip phase of each mode is a unique integer multiple of 2π . When the right mirror is frequency dependent, we can still think of the branches as different longitudinal modes, but the total round-trip phase is not necessarily a unique number. This is due to the phase $\arg[r_R(\omega)]$, which especially affects the modes near the resonance.

The name ‘‘instantaneous modes’’ is taken from analogous concepts in Refs. [11,37–39], and refers to the fact that they solve the oscillation condition for a fixed instantaneous carrier density. That is, the instantaneous modes are the resonant modes in the system if we freeze the carrier density at a particular instant in time. They may be leaky or amplified and are characterized by complex frequencies.

The imaginary part of an instantaneous mode gives the effective net modal gain per unit time $\bar{G}_n(N) = 2 \text{Im}[\tilde{\omega}_n(N)]$, and we define the modal differential gain per unit time as $\bar{G}_{Nn}(N) = \frac{d}{dN} \bar{G}_n(N)$. In this paper, ‘‘effective’’ parameters are characterized with an overline.

In Fig. 2(a) the instantaneous modes are drawn as the red (dark gray) and blue (light gray) continuous curves in $(\Delta\nu, N)$ space, where $\Delta\nu = [\text{Re}(\tilde{\omega}) - \omega_c]/2\pi$, using the example of a single-cavity Fano laser with a Lorentzian reflection spectrum $r_R(\omega) \propto 1/(\omega - \omega_c - i\gamma)$ [17]. Blue (red) means the mode

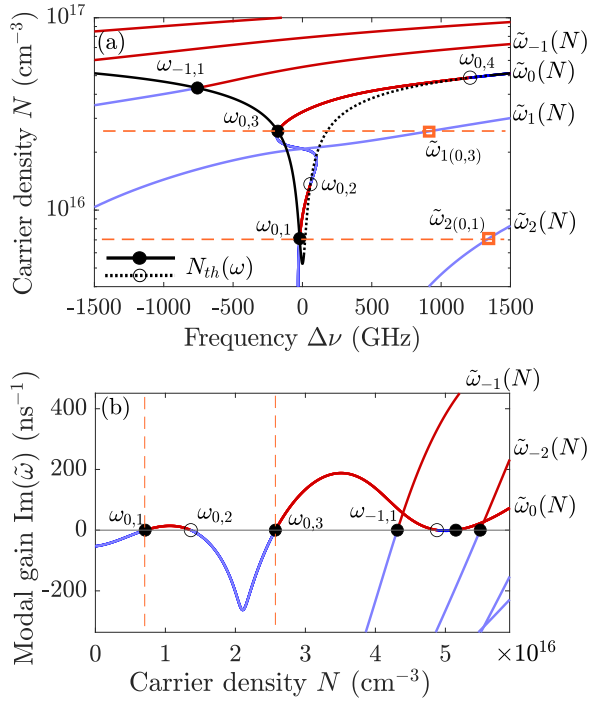


FIG. 2. Illustration of the various concepts introduced in Sec. II in the (a) $(\Delta\nu, N)$ plane and (b) $[N, \text{Im}(\tilde{\omega})]$ plane, using an example of a Fano laser with a Lorentzian reflection spectrum. The frequency axis in (a) is shifted relative to the reflectivity peak $\Delta\nu = [\text{Re}(\tilde{\omega}) - \omega_c]/2\pi$. The blue (light gray) and red (dark gray) continuous curves are instantaneous modes $\tilde{\omega}_n(N)$, with $\text{Im}(\tilde{\omega}) > 0$ in red and $\text{Im}(\tilde{\omega}) < 0$ in blue. The black curve in (a) is the threshold carrier density $N_{th}(\omega)$ as a function of (real) frequency, which is continuous when $\bar{\Gamma}(\omega) > 0$ and dotted when $\bar{\Gamma}(\omega) < 0$, following Eq. (14). Steady-state modes are shown as black dots, and antimodes are empty circles. For the two lowest-threshold steady-state modes, $s = (0, 1)$ and $s = (0, 3)$, the horizontal dashed orange lines indicate their threshold carrier densities, and orange squares indicate sidemodes. Only the sidemodes of the two lowest steady-state modes are indicated in order not to crowd the plot.

is below (above) threshold, as illustrated in Fig. 2(b), which shows the modal gain $\bar{G}_n(N)$ as a function of carrier density.

The points where $\tilde{\omega}_n(N)$ become real-valued, such that $\bar{G}_n(N) = 0$, define the steady-state solutions (ω_s, N_s) which satisfy the oscillation condition

$$r_L(\omega_s, N_s)r_R(\omega_s) = 1, \quad (\omega_s, N_s) \in \mathbb{R}^2. \quad (7)$$

In the time domain, the steady-state solutions correspond to continuous-wave (CW) operation at a certain frequency and carrier density. The subscript “ s ” here denotes a set of two indices, $s = (n, j)$, corresponding to the j th steady-state solution belonging to the n th instantaneous mode, $\omega_{n,j} = \tilde{\omega}_n(N_{n,j})$.

The steady-state solutions can further be divided into *steady-state modes* and *antimodes*, depending on whether the associated effective gain crosses zero in the positive [$\bar{G}_{N_n}(N_s) > 0$] or negative [$\bar{G}_{N_n}(N_s) < 0$] direction. In Figs. 2(a) and 2(b), steady-state modes are marked with filled circles, while antimodes are marked with empty circles. Only the steady-state modes can be stable, while

antimodes are always unstable and correspond to saddle nodes [40].

As shown in Fig. 2(a), all steady-state solutions (ω_s, N_s) fall on the line $N_{th}(\omega)$, which solves the amplitude condition $|r_L[\omega, N_{th}(\omega)]r_R(\omega)| = 1$. The shape of $N_{th}(\omega)$ mimics the reflection spectrum $r_R(\omega)$, and is given by

$$\Gamma g[N_{th}(\omega)] = \alpha_i + \frac{1}{2L} \ln \left(\frac{1}{|r_1 r_R(\omega)|^2} \right), \quad (8)$$

where Γ is the confinement factor, $g(N)$ is the material gain, α_i represents intrinsic losses in the waveguide, and r_1 is the reflectivity of the left broadband mirror. The actual positions of steady-state modes are then given by the phase condition along the threshold carrier density curve,

$$\arg\{r_R(\omega_s)\} + \arg\{r_L[\omega_s, N_{th}(\omega_s)]\} = 2\pi p + \phi_0, \quad (9)$$

where p is an integer, and ϕ_0 is a global phase representing the possible inclusion of some phase tuning mechanism. Numerically, looking for solutions to the phase condition along the threshold carrier density curve makes finding the steady-state solutions a simple task. The instantaneous modes can then be computed numerically with path continuation starting from each steady-state solution.

Finally, if we consider a particular steady-state solution (ω_s, N_s) belonging to the n th instantaneous mode $s = (n, j)$, then we define its *sidemodes* $\tilde{\omega}_{ms} \equiv \tilde{\omega}_m(N_s)$ as the other instantaneous modes, $m \neq n$, evaluated at the particular steady-state carrier density N_s . Here, the subscripts “ ms ” should be read as the m th sidemode of the steady-state solution s . The sidemodes thus solve the oscillation condition at the carrier density level $N = N_s$,

$$r_L(\tilde{\omega}_{ms}, N_s)r_R(\tilde{\omega}_{ms}) = 1, \quad s = (n, j), m \neq n. \quad (10)$$

If the laser oscillates in the steady-state mode s , then the threshold carrier density N_s of that mode defines a particular set of resonant modes that are simultaneously present in the system, i.e., the sidemodes. The sidemodes play an important role in the dynamics and the stability of the lasing mode, and in particular, they may lead to “photon-photon resonances” in the small-signal modulation response [11,37,40,41].

In Fig. 2(a) the sidemodes can be located by focusing on a particular steady-state solution and looking horizontally at other instantaneous modes. This is indicated by orange dashed lines for the two lowest-threshold steady-state modes $\omega_{0,1}$ and $\omega_{0,3}$, which both have a single sidemode, $\tilde{\omega}_{2(0,1)}$ and $\tilde{\omega}_{1(0,3)}$, within the limits of the real frequency axis. The imaginary parts of the sidemodes determine whether they are damped [$\text{Im}(\tilde{\omega}_{ms}) < 0$, below threshold] or undamped [$\text{Im}(\tilde{\omega}_{ms}) > 0$, above threshold]. Looking at the imaginary parts in Fig. 2(b), the sidemodes are seen vertically from the associated steady-state mode. All sidemodes are damped for both $\omega_{0,1}$ and $\omega_{0,3}$, while e.g., $\omega_{-1,1}$ have an undamped sidemode on the $\tilde{\omega}_0$ branch.

To briefly illustrate the importance of sidemodes, consider what happens as the pump rate is increased from below to above threshold of a particular steady-state mode (ω_s, N_s) . Letting R_p denote the pump rate and τ_s the carrier lifetime, then immediately above the threshold $R_p \gtrsim N_s/\tau_s$, its stability is determined by the positions of the sidemodes. If just one sidemode experiences gain, $\text{Im}(\tilde{\omega}_{ms}) > 0$, the steady-state

mode (ω_s, N_s) is unstable; otherwise it is stable [40]. This means $\omega_{0,1}$ and $\omega_{0,3}$ in Fig. 2 are both stable at threshold, since all their respective sidemodes are below threshold.

Further, as the pump rate is increased above threshold, a steady-state mode which is initially stable may become unstable due to, e.g., the presence of a weakly damped sidemode. Similarly, steady-state modes, which are initially unstable but only weakly suppressed, may become stable. These mode-coupling phenomena are sometimes referred to as dynamic instability and dynamic stability, respectively [40,42]. This phenomenon of dynamic instability has also been addressed theoretically and experimentally for two coupled photonic-crystal lasers in Ref. [43].

In order to find the instantaneous modes, the wave number $k(\omega, N) = k(\omega_r, N_r) + \Delta k(\omega, N)$ is expanded as

$$2i\Delta kL \approx \frac{1}{2}(1 - i\alpha)\Gamma v_g[g(N) - g(N_s)]\tau_L + i(\omega - \omega_s)\tau_L, \quad (11)$$

where Γ is the confinement factor, v_g is the group velocity, $\tau_L = 2L/v_g$ is the round-trip time in the active section, and α is the linewidth enhancement factor. The reference point (ω_r, N_r) can be any steady-state mode.

Returning to the instantaneous modes, they can be shown to satisfy

$$\frac{d\tilde{\omega}}{dN} = \frac{\tau_L}{\tau_L + \tau_R(\tilde{\omega})} \times \frac{1}{2}(i + \alpha)\Gamma v_g g_N, \quad (12)$$

where $g_N = g_N(N)$ is the material differential gain. Furthermore, $\tau_R(\omega)$ is a complex time defined the same way as in Ref. [44] by

$$\tau_R(\omega) \equiv -i \frac{d}{d\omega} \ln r_R(\omega). \quad (13)$$

Its real part corresponds to an effective round-trip time in the PDR given by the frequency derivative of the phase. In contrast, the imaginary part leads to additional phase-amplitude coupling. Compared to the case without a PDR, $\frac{d\omega}{dN}$ is modified by a factor $\tau_L/[\tau_L + \tau_R(\omega)]$, which appears as a complex-valued weighting or confinement factor [39]. Thus, we can define an effective confinement factor $\bar{\Gamma}(\omega)$ and an effective linewidth enhancement factor $\bar{\alpha}(\omega)$ by

$$\bar{\Gamma}(\omega)[i + \bar{\alpha}(\omega)] \equiv \frac{\Gamma(i + \alpha)}{1 + \tau_R(\omega)/\tau_L}. \quad (14)$$

With these definitions, we get

$$\frac{d\tilde{\omega}}{dN} = \frac{1}{2}[i + \bar{\alpha}(\tilde{\omega})]\bar{\Gamma}(\tilde{\omega})v_g g_N. \quad (15)$$

Defining a general differential gain function $\bar{G}_N(\tilde{\omega}, N) \equiv \bar{\Gamma}(\tilde{\omega})v_g g_N(N)$, the modal differential gain for the n th instantaneous mode is $\bar{G}_{N_n}(N) = \bar{G}_N[\tilde{\omega}_n(N), N]$. Due to the frequency dependence of the PDR, $\bar{\Gamma}(\omega)$ and $\bar{\alpha}(\omega)$ will vary between the different steady-state solutions. The condition for a steady-state solution (ω_s, N_s) to be an antimode can now be expressed as

$$\bar{G}_N(\omega_s, N_s) \propto \bar{\Gamma}(\omega_s) < 0 \quad (\text{antimodes}), \quad (16)$$

while steady-state modes have $\bar{\Gamma}(\omega_s) > 0$.

We note that similar effective parameters have been derived in Refs. [44,45], with the slight difference that instead of $\bar{\Gamma}(\omega)$, Ref. [45] defines an effective relaxation oscillation frequency, while Ref. [44] defines an effective photon lifetime.

Here, we take the effective confinement factor to be more fundamental as, arguably, the effect on the photon lifetime and the relaxation oscillation frequency is *because* of the modified confinement in the active section. Further, if the PDR is only weakly dispersive, such that $\tau_R(\omega)$ can be approximated by its steady-state value, $\tau_R(\omega_s)$, for a particular steady-state frequency ω_s , the dynamics will be qualitatively similar to a conventional Fabry-Perot laser, but with the rescaled parameters $\bar{\Gamma}(\omega_s)$ and $\bar{\alpha}(\omega_s)$. In this weakly dispersive limit, the PDR results in a scaling of the modal differential gain $\bar{G}_N = \bar{\Gamma}(\omega_s)v_g g_N$, the linewidth, the relaxation oscillation frequency $\bar{\omega}_R = \sqrt{(R_p/R_{p,th} - 1)\bar{G}_N N_s/\tau_s}$, and the photon lifetime $\bar{\tau}_p = [\bar{\Gamma}(\omega_s)v_g g_{th}]^{-1}$, where $g_{th} = g[N_{th}(\omega_s)]$ is the material threshold gain. These expressions agree with Refs. [37,39,44,45].

B. Dynamical model

The model we use is based on the iterative model in Ref. [36] and also used in Ref. [12]. We define the slowly varying envelopes $A(t)$ and $A_-(t)$ by

$$A_{(-)}(t)e^{-i\omega_r t} = \frac{1}{2\pi} \int_0^\infty E_{(-)}(\omega)e^{-i\omega t} d\omega. \quad (17)$$

Using this definition of the Fourier transform along with the wave-number expansion in Eq. (11), Eq. (3) can be transformed into the time domain to give expressions for $A(t)$ and $A_-(t)$,

$$A(t) = e^{\frac{1}{2}(1-i\alpha)\Gamma v_g [g(N) - g(N_r)]\tau_L} \times \frac{A_-(t - \tau_L)}{r_R(\omega_r)} + F(t), \quad (18)$$

where $F(t)$ is the inverse Fourier transform of $F(\omega)$, and $\langle g(N) \rangle(t)$ is the gain averaged over one round trip in the laser cavity,

$$\langle g(N) \rangle = \frac{1}{\tau_L} \int_{t-\tau_L}^t g[N(t')] dt'. \quad (19)$$

The reflected field $A_-(t)$ is given formally by

$$A_-(t) = \int_{-\infty}^t \hat{r}_R(t - t') A(t') dt', \quad (20)$$

where $\hat{r}_R(t)$ is the impulse response function of the PDR, which is the inverse Fourier transform of $r_R(\omega)$, using the same definition as in Eq. (17). We remark that the form of $A_-(t)$ given in Eq. (20) is used solely for analysis. For numerical simulations, it is advantageous to describe $A_-(t)$ in terms of a rate equation derived from, e.g., coupled-mode theory. Finally, the evolution of the carrier density is described by the rate equation

$$\frac{d}{dt} N = R_p - \frac{N}{\tau_s} - v_g g(N) N_p. \quad (21)$$

Here, N_p is the photon number density. In steady state, $N_p \propto |A|^2$ with a proportionality constant given in Ref. [46]. Assuming this proportionality to hold out of equilibrium, we normalize $|A|^2 = N_p$.

C. Relaxation oscillations

Next, we perform a linear stability analysis of the steady-state modes fulfilling $\bar{\Gamma}(\omega_s) > 0$. A key result regards the

impact of a dispersive mirror on the relaxation oscillations. Relaxation oscillations are intensity oscillations that occur due to coupling between the carrier- and photon reservoirs. The linear stability analysis is carried out by assuming perturbations from steady state with characteristic time dependence $e^{-i\Omega t}$. The real part $\text{Re}(\Omega)$ gives the angular frequency, and $\text{Im}(\Omega) < 0$ corresponds to damped oscillations, while $\text{Im}(\Omega) > 0$ means the oscillations are undamped. For a steady-state mode to be stable, no eigenvalue Ω can have a positive imaginary part.

For conventional Fabry-Perot lasers, the frequency and damping rate of relaxation oscillations are determined by a characteristic equation of the form [47]

$$-\Omega^2 - i\gamma_R\Omega + \omega_R^2 = 0, \quad (22)$$

where the damping rate γ_R and relaxation resonance frequency ω_R are given by

$$\gamma_R = \frac{1}{\tau_s} + \tau_p\omega_R^2, \quad \omega_R^2 = \Gamma v_g g_N \left(R_p - \frac{N_s}{\tau_s} \right). \quad (23)$$

Here, $\tau_p = (\Gamma v_g g_{th})^{-1}$ is the photon lifetime, where $g_{th} = g(N_s)$ is the material threshold gain. For lasers with dispersive mirrors, we can derive a generalization of the above characteristic equation to include the effect of a frequency-dependent mirror (see Appendix B for the details)

$$-\Omega^2 - i\gamma_R\Omega + \frac{1}{2}\omega_R^2[H(\Omega) + H^*(-\Omega^*)] = 0, \quad (24)$$

where $H(\Omega)$ is given by

$$H(\Omega) = (1 - i\alpha) \frac{e^{i\Omega\tau_L} - 1}{\frac{r_R(\omega_s + \Omega)}{r_R(\omega_s)} e^{i\Omega\tau_L} - 1}. \quad (25)$$

The combined transfer function $H_P(\Omega) = [H(\Omega) + H^*(-\Omega^*)]/2$ relates the power to the carrier density, i.e., $-i\Omega\delta P(\Omega) \propto H_P(\Omega)\delta N(\Omega)$. Physically, the two terms take into account that intensity oscillations at a frequency Ω generate two optical sidebands at the frequencies $\omega_s \pm \Omega$. If the reflectivity depends on frequency, these optical sidebands will experience different loss and phase delays.

Equation (24) cannot be solved analytically in general. However, if $|\Omega|$ is sufficiently small compared to the characteristic frequency scales in $r(\omega_s + \Omega)$ as well as the inverse round-trip time τ_l^{-1} , then we may expand $H(\Omega) \simeq H(0) + \Omega H'(0)$. For example, in the case of the coupled-cavity Fano laser with the reflectivity given by Eq. (1), the approximation requires $|\Omega| \ll |\omega_s - \omega_{\pm} + i\gamma_{\pm}|$. This allows us to define approximate relaxation resonance frequencies and damping rates by

$$\bar{\omega}_R^2 \equiv \omega_R^2 \text{Re}[H(0)], \quad (26)$$

$$\bar{\gamma}_R \equiv \gamma_R - \omega_R^2 \text{Im}[H'(0)], \quad (27)$$

where the prime denotes the derivative with respect to Ω . The characteristic equation then becomes

$$-\Omega^2 - i\bar{\gamma}_R\Omega + \bar{\omega}_R^2 = 0. \quad (28)$$

We have

$$H(0) = \frac{1 - i\alpha}{1 + \tau_R(\omega_s)/\tau_L} = \frac{\bar{\Gamma}(\omega_s)}{\Gamma} [1 - i\bar{\alpha}(\omega_s)], \quad (29)$$

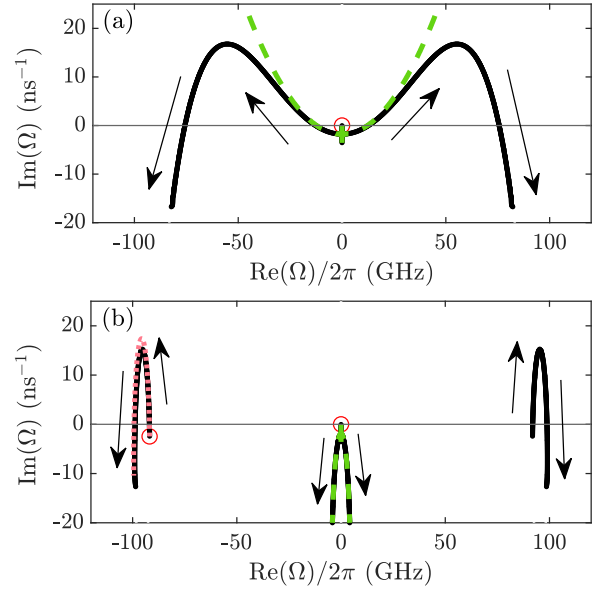


FIG. 3. Evolution of the eigenvalues of the linearization related to the lowest-threshold steady-state mode as the pump rate is varied for the case of (a) dispersive self- Q -switching and (b) beating oscillations. The green dashed curves show the approximation in Eqs. (26) and (27), while the pink dotted curve shows the approximation in Eq. (32). The red circles show the positions of the sidemodes $\Omega = \bar{\omega}_{ms} - \omega_s$.

where we recall $\tau_R(\omega) = -i\partial_\omega \ln r_R(\omega)$, and

$$H'(0) = \frac{1}{2} \tau_L (\alpha + i) \frac{r_R''(\omega_s)/r_R(\omega_s)}{[\tau_L + \tau_R(\omega_s)]^2}. \quad (30)$$

Remarkably, the approximation for the relaxation oscillation frequency matches the usual expression if the rescaled confinement factor is used.

The eigenvalues are, in general, functions of the pump rate. As an example, in Fig. 3 we consider two sets of parameters for the coupled-cavity Fano laser given in Table I, which are also used later in Secs. III and IV, and plot the traces of the eigenvalues in the complex plane as the pump rate varies. The exact solutions to Eq. (24) are given in black, while the approximations to the relaxation oscillation eigenvalues are given in dashed green, showing good agreement for $\text{Re}(\Omega)/2\pi \lesssim 30$ GHz. The points where the eigenvalues cross the real axis, $\text{Im}(\Omega) = 0$, correspond to Hopf bifurcations.

This general analytical result can be applied to a large class of lasers and can be used to explain a number of results presented in the literature. Reference [48] considers the case of a single-cavity Fano laser without a blocking hole in the waveguide and where the lasing frequency coincides exactly with the resonance peak of the cavity. Their results on the relaxation oscillation frequency and damping rate agree with the expressions above, and furthermore, we can now easily evaluate the influence of detuning and the presence of a blocking hole. Another example is a laser with weak optical feedback with an effective reflectivity that can be approximated as $r_R(\omega) = r_2[1 + \kappa \exp(i\omega\tau)]$, where κ is the feedback strength and τ is the round-trip time in the feedback

TABLE I. Parameters used in simulation. Parameters outside (inside) of parentheses are specific to simulations presented in Sec. III (IV). Material parameters are based on Ref. [18]. We acknowledge that the value for the carrier density is rather low, while the value for the differential gain is rather high. The important quantity for the dynamics, however, is the product $g_N N_0$, which is at a high but realistic level.

Parameter	Symbol	Value
Material differential gain	g_N	$5 \times 10^{-12} \text{ cm}^2$
Transparency carrier density	N_0	$5 \times 10^{15} \text{ cm}^{-3}$
Carrier lifetime	τ_s	0.28 ns
Confinement factor	Γ	0.01
Left mirror reflectivity	r_1	-0.99
Waveguide losses	α_i	10 cm^{-1}
Reference length of laser cavity	L	$4.98 \mu\text{m}$
Reference refractive index	n_r	3.5
Reference group index	n_g	3.5
Linewidth enhancement factor	α	3.3
Parameters related to PDR		
Reference wavelength	λ_r	1554 nm
Cavity 1 resonance frequency	ω_{c1}	$2\pi c/\lambda_r$
Cavity 2 detuning from ω_{c1}	Δ	0 (-100) GHz
Vertical scattering Q	Q_i	10^5
Cavity-waveguide Q	Q_w	750
Decay rate related to channel x	γ_x	$(2\pi c/\lambda_r)/2Q_x$
Evanescent coupling rate	μ	0.65 (0) γ_w
Indirect coupling phase	θ	$-\pi/6$ (0)
Fundamental steady-state mode	ω_{s0}	$\omega_{c1} + 0.65 \gamma_w$ (ω_{c1})

arm. In this case,

$$\text{Re}[H(0)] = \frac{1 + \frac{\kappa\tau}{\tau_L} [\cos(\omega_s\tau) - \alpha \sin(\omega_s\tau)]}{1 + \left(\frac{\kappa\tau}{\tau_L}\right)^2 + 2\frac{\kappa\tau}{\tau_L} \cos(\omega_s\tau)}, \quad (31)$$

which agrees with the modification of the relaxation oscillation frequency given in Ref. [49].

Returning to the general analysis, we observe that the second derivative $r_R''(\omega_s)$ is decisive for the stability. In the case where $|r_R(\omega)|$ is at an extremum, we have $\text{Im}[H'(0)] \propto \alpha(\arg r_R)'' + (\ln |r_R|)'' - (\arg r_R)^2$. This shows that the damping rate of relaxation oscillations increases near the maximum of a reflection peak while it decreases near a minimum. In fact, the second and third terms have clear physical interpretations, corresponding to spectral filtering and amplification and increased storage time in the passive section. This agrees with the results and physical interpretations given in Ref. [23], showing that a Fano laser operating at the reflection peak has increased tolerance toward external feedback.

Finally, a positive curvature of the reflection spectrum leads more readily to instabilities. In Ref. [13], the authors analyze self-pulsing in a laser with reflection from a chirped grating, and they also conclude that the phase curvature is decisive for the stability. This insight can be used as a guideline for designing self-pulsing lasers based on dispersive mirrors.

D. Photon-photon resonances

In addition to the eigenvalues of Eq. (24) that relate to relaxation oscillations, another set of eigenvalues is related to coupling between the steady-state mode and sidemodes. We

notice that $H(\Omega)$ has poles at the positions of the sidemodes relative to the steady-state mode, $\Omega_{\text{ms}} = \tilde{\omega}_{\text{ms}} - \omega_s$. Just above threshold, where $\omega_R^2 \sim 0^+$ is negligible, the poles Ω_{ms} are exact eigenvalues. When further increasing the pump rate, the eigenvalues move in the complex plane.

Writing $\Omega = \Omega_{\text{ms}} + \Delta\Omega$, we can get the approximate expression

$$\Delta\Omega \approx \frac{\frac{1}{2}\omega_R^2}{\gamma_R - i\Omega_{\text{ms}}} \times \frac{1 - i\alpha}{1 + \tau_R(\tilde{\omega}_{\text{ms}})/\tau_L} \times \frac{e^{i\Omega_{\text{ms}}\tau_L} - 1}{i\Omega_{\text{ms}}\tau_L}, \quad (32)$$

which is valid for $|\Delta\Omega| \ll |\Omega_{\text{ms}}|$. The key point here is that the first factor gives rise to an asymmetric mode coupling, which dampens sidemodes on the blue side [$\text{Re}(\Omega_{\text{ms}}) > 0$] and amplifies sidemodes on the red side [$\text{Re}(\Omega_{\text{ms}}) < 0$]. This four-wave mixing effect, mediated by carrier oscillations, is known as the Bogatov effect [42]. The effect is responsible for the onset of beating oscillations (where the lowest-threshold “blue” mode becomes unstable), as well as the termination of beating oscillations due to so-called dynamic stability of the “red” mode with higher threshold [40]. In Ref. [43], the authors show that the effect can also be used to transfer energy from the blue mode to the red mode in the case of two coupled photonic crystal cavities.

Figure 3(b) shows an example of a case where a pair of eigenvalues related to photon-photon resonances cross the real axis, leading to instability. Specifically, we consider the eigenvalues of the lowest-threshold steady-state mode for the laser in Sec. IV, which has a weakly damped sidemode near -93 GHz (red circle). When the pump rate is increased above the lasing threshold, the eigenvalues related to this sidemode move upward and become unstable. The approximation given in Eq. (32) is shown as the dotted pink line in Fig. 3(b), indicating good agreement with the numerical result.

III. APPLICATION: SELF-Q-SWITCHING

We now apply the general results derived above to the coupled-cavity Fano laser [see Fig. 1(a)], which provides a general platform to tailor the mirror dispersion. First, we consider the possibility of self- Q -switching, i.e., the instability related to relaxation oscillations leading to the self-pulsing shown in Fig. 4(a).

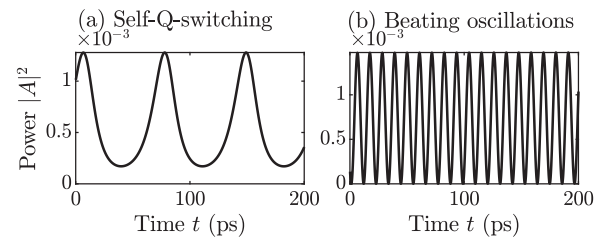


FIG. 4. Time traces of the normalized power in the active section during (a) dispersive self- Q -switching and (b) beating-type oscillations. In (a), we observe a train of pulses with pulse widths of ~ 20 ps and repetition rate of ~ 15 GHz. In (b), we observe beating oscillations, which in the frequency domain corresponds to dual-mode (or two-color) lasing. We observe fast (~ 93 GHz) sinusoidal oscillations that result from the beating between two modes lasing simultaneously, which are locked together through carrier oscillations in the active medium.

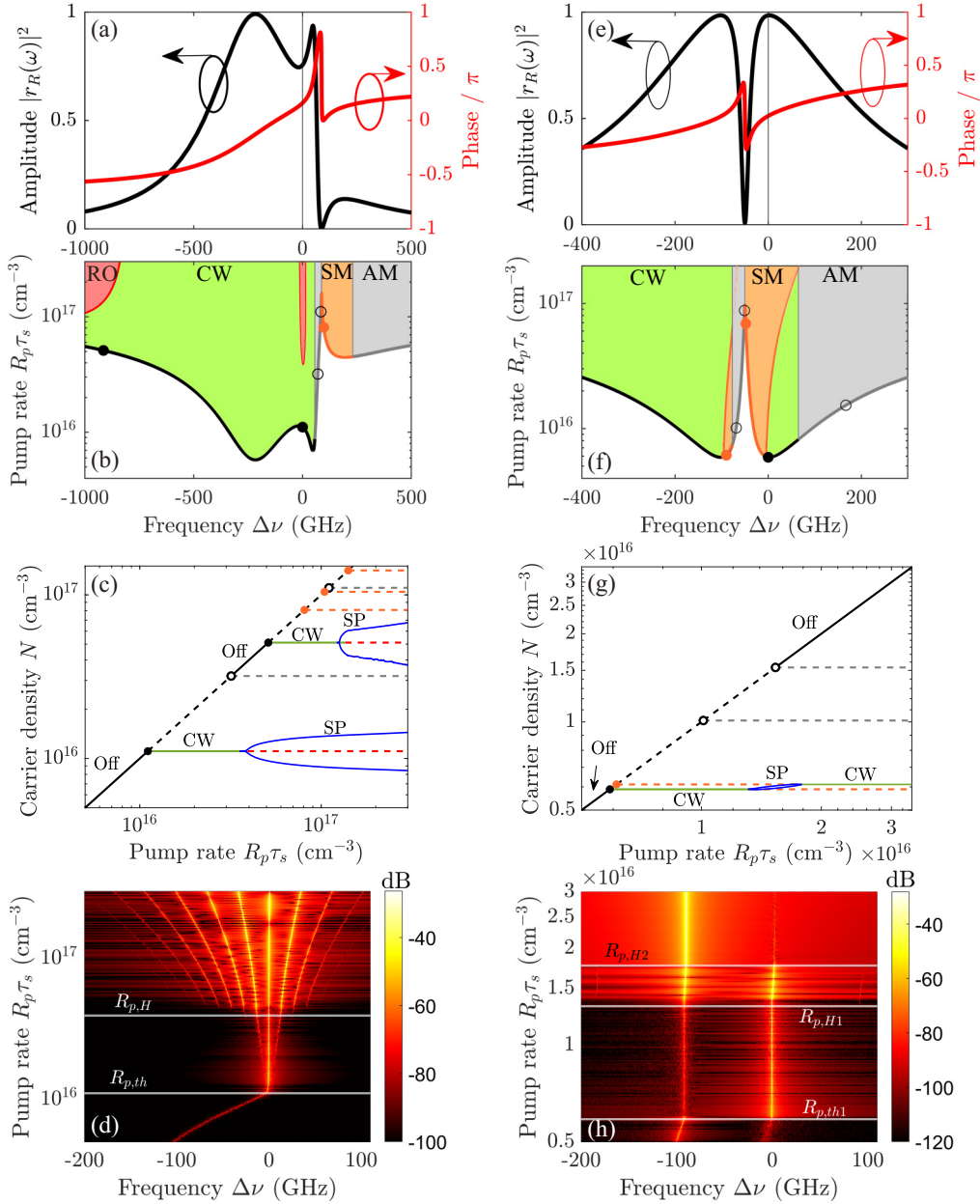


FIG. 5. Figures related to self- Q -switching in the first column (a)–(d) and beating oscillations in the second column (e)–(h). (a and e) Mirror reflectivities $r_R(\omega)$ with $|r_R(\omega)|^2$ in black (left axes) and $\arg[r_R(\omega)]/\pi$ in red (right axes). (b and f) Stability diagram in terms of frequency and pump rate, showing the lasing threshold as a function of frequency, the various steady-state solutions, and the boundary for self-pulsing. Description in the main text. (c and g) Bifurcation diagrams with N vs R_p . (d and h) Optical spectrum in color scale for varying pump rate.

Knowing that we need a positive curvature, we choose parameters that lead to the reflection spectrum in Fig. 5(a), where $|r_R(\omega)|^2$ is shown in black (left axis) and $\phi(\omega)$ is shown in red (right axis). The frequency axis is $\Delta\nu = (\omega - \omega_{s0})/2\pi$, where the vertical line at $\Delta\nu = 0$ indicates the targeted steady-state frequency ω_{s0} used in simulations unless otherwise specified.

Figure 5(b) shows a stability diagram of steady-state solutions in frequency ω_s and pump rate R_p . The white region is below the lasing threshold $R_p < N_{th}(\omega)/\tau_s$, while the colored regions are above threshold. Further, the color indicates the stability of steady-state solutions in that region, and if unsta-

ble, whether the undamped eigenvalues [$\text{Im}(\Omega) > 0$] can be attributed to relaxation oscillations (red, RO), unsuppressed sidemodes (orange, SM), or antimodes (AM, gray). Green (CW) denotes regions of stable CW lasing where all eigenvalues have negative imaginary parts. We indeed observe that the self-pulsing threshold for undamped relaxation oscillations is lowest near the point where $|r_R(\omega)|^2$ has the largest positive curvature. Additionally, the circle markers on the lasing threshold border indicate the frequencies $\{\omega_s\}$ of the particular set of steady-state solutions that coexist with a steady-state mode at the indicated target frequency $\omega_s = \omega_{s0}$. That is, inserting $\omega_s = \omega_{s0}$ in the phase condition Eq. (9) fixes the

required global phase ϕ_0 , which in turn determines all other steady-state solutions.

Figure 5(c) shows the bifurcation diagram in the (R_p, N) plane for a choice of global phase giving rise to the steady-state solutions indicated in Fig. 5(b). As the pump rate varies, the lines show the position and stability of the various fixed points and limit cycles. A continuous line denotes a stable state with the type being indicated [off-state in black, CW in green, and self-pulsing (SP) in blue]. A dashed line represents an unstable state. The black diagonal, $N = R_p \tau_s$, is the off-state corresponding to a solution with zero photons in the cavity. It is stable if all the instantaneous modes are below threshold at $N = R_p \tau_s$, i.e., $\text{Im}[\tilde{\omega}_n(R_p \tau_s)] < 0$ for all n . The horizontal lines are steady-state solutions. For the self-pulsing states, the blue curves denote the limit cycle's maximum and minimum carrier density. Note that we are only considering deterministic dynamics here, so spontaneous emission noise is neglected. Finally, we note that the curve corresponding to the limit cycle at higher carrier density is slightly jagged due to the dynamics not being a simple period-one limit cycle but containing additional frequency components.

We observe that the lowest-threshold mode is initially globally attracting but becomes unstable through a Hopf bifurcation, giving rise to self-pulsing. Additionally, we observe the existence of pump regimes where (1) a stable CW-state coexists with a stable off-state, (2) a stable limit cycle coexists with a stable off-state, (3) a stable limit cycle coexists with a stable CW state, and (4) only nonstationary states exist. This shows the rich landscape of possible dynamics in the system. The various kinds of multistable regimes could also be attractive for switching applications or for excitable behavior [50].

Figure 5(d) shows a 2D map of the evolution of the optical spectrum as a function of the pump rate, computed by numerical integration of the dynamical equations and including Langevin noise. Below the threshold for self-pulsing, the two sidebands arising from relaxation oscillations can be observed. Above the self-pulsing threshold at $R_p \approx 3.5R_{p,th}$, we observe the formation of a frequency comb. As the pump rate further increases, more and more comb lines become visible, which can be interpreted as four-wave mixing of the relaxation oscillation sidebands and the carrier frequency. In the time domain, this corresponds to self-pulsing, which manifests as sinusoidal temporal modulation of the power at the onset of the instability, evolving into a train of pulses when the pump rate is increased. The dynamics are shown in Fig. 4(a), for a pump rate well above the onset of self-pulsing. Typical pulse widths are on the order of ~ 10 – 20 ps, and repetition rates are on the order of ~ 10 – 20 GHz.

IV. APPLICATION: BEATING OSCILLATIONS

The second application we consider is the realization of a dual-mode laser, which exhibits beating oscillations [see Fig. 4(b)]. This type of self-pulsing consists of fast sinusoidal oscillations with a frequency in the range of ~ 20 – 200 GHz, which can be tuned by the design of the passive reflector. Physically, this type of dynamics is interpreted as the beating between two modes that lase simultaneously and are locked together through carrier oscillations in the active medium.

The requirement for beating oscillations is a weakly damped sidemode, which is red-detuned from the lowest-threshold steady-state mode [40,42].

We achieve beating oscillations with the reflectivity spectrum in Fig. 5(e), where the two cavity supermodes are spectrally aligned, thus inducing a narrow transparency window where they overlap due to destructive interference. As such, this is an example of electromagnetically induced transparency (EIT) in optical microcavities [51]. The EIT resonance arises due to strong Fano interference, that is, interference between different optical pathways. Importantly, the EIT resonance is accompanied by a small wiggle or undulation of the phase response. Due to the negative group delay within the transparency window, the phase condition can be satisfied on both sides of the transparency window.

In Fig. 5(f), we observe two steady-state modes with comparable thresholds, with the mode on the blue side (black dot) having a slightly lower threshold. We observe that the steady-state mode at $\Delta\nu = 0$ becomes unstable above a certain threshold when the pump rate crosses into the orange region. On the other hand, the steady-state mode in the orange region on the red side, which is initially unstable, becomes stable at even higher pump rates. Of course, this boundary collides with the laser threshold curve at the point where the two modes have identical thresholds.

Conversely, when the lowest threshold mode is on the red side, it is always stable. In the present case, the coupling between these two modes is what gives rise to the dual-mode operation. Further, the beat note frequency is approximately given by the detuning Δ between the two cavities constituting the dispersive laser mirror. This parameter can be tuned dynamically by electro-optic means or through design by modifying the cavity geometry.

Figure 5(g) shows the bifurcation diagram. Again, we observe various kinds of multistable behavior, but most importantly, there is a window between the instability of the lowest threshold mode and the dynamic stability of the second-lowest mode where beating oscillations occur.

Figure 5(h) shows the optical spectrum. The blue mode starts to lase at $R_{p,th1}$, and we observe single-mode lasing until $R_p = R_{p,H1}$, which constitutes the onset of dual-mode lasing. At $R_p = R_{p,H2}$, the red mode becomes stable, and the dual-mode lasing stops. Due to the inclusion of Langevin noise in the simulations, outlines of both the red and blue modes can be observed even when they do not lase.

Finally, we remark that the two steady-state modes are resonant with different cavities, meaning that the photon densities in the two cavities differ strongly and depend on the oscillating mode. Therefore, if the two cavities are coupled to different cross-ports, the two steady-state modes will have different output channels. Deliberately inducing mode-hopping could then be used as a routing mechanism.

V. DISCUSSION

Comparing the coupled-cavity Fano laser to earlier demonstrations and predictions of self-pulsing lasers, we wish to highlight a few points. In Refs. [43,52,53], the authors experimentally and theoretically investigate symmetric coupled-cavity laser systems consisting of two coupled

photonic crystal lasers. In Ref. [52] the authors demonstrate spontaneous mirror symmetry breaking above a certain pump rate, where the energy distribution will become asymmetric and mainly concentrated in a single cavity. Additionally, they predict regimes where the power will spontaneously oscillate back and forth between the two nanocavities. Compared to the present case, a major difference is that the two nanocavities are both active and form two complete laser cavities, while in our case, the coupled cavities are passive and merely work as a frequency-dependent mirror. The mechanism for self-pulsing in Ref. [52] is thus attributed to an ac Josephson-like effect, although the mechanism appears somewhat similar to beating oscillations.

In Refs. [43,53], the authors demonstrate switching between the bonding and the antibonding supermode mediated by a region of beating oscillations. As in our case, the direction of the mode-coupling is from the blue mode to the red mode and the mechanism is attributed to a Bogatov effect, but it relies on the presence of two different active sites rather than a dispersive reflector.

If we compare the coupled-cavity Fano laser in the self- Q -switched regime to other self-pulsing lasers with dispersive mirrors, such as the hybrid laser in Ref. [12] or qualitatively similar devices in Refs. [14,54], the frequency combs also emerge through undamped relaxation oscillations. Due to the size of those macroscopic structures, they also produce much higher output power. On the other hand, the Fano laser allows extreme miniaturization and a lower threshold. It should be noted that in contrast to the dispersive self- Q -switching discussed in Sec. III, the beating-type oscillations can also occur in lasers that are not based on PDRs. An example is the self-pulsing square-microcavity laser in Ref. [55], where mode-coupling occurs through spatial hole-burning, leading to a spatial modulation of the refractive index.

VI. CONCLUSION

In conclusion, we have presented a general analysis of lasers incorporating a passive dispersive mirror. The analysis can be used to study a large class of lasers, and the insights can be applied to tailor the dynamics of lasers. In particular, we applied the model to a different laser geometry, which provides a flexible platform for realizing many different types of cavity dispersion. In combination with simulations, e.g., using FDTD, of the reflection spectrum in specific devices, the model can be used as a design guideline. Finally, the model may serve as a starting point for extending the formalism to study *active* dispersive mirrors, where the gain and refractive index vary in time due to nonlinearities in the cavities or the presence of active material.

ACKNOWLEDGMENTS

This work was supported by the Danish National Research Foundation (Grant No. DNRF147 - NanoPhoton) and by the European Research Council (Grant No. 834410 FANO). M.H. and Y.Y. acknowledge the support from Villum Foundation via the Young Investigator Programme (Grants No. 37417 - QNET-NODES and No. 42026 - EXTREME).

APPENDIX A: THE COUPLED-CAVITY FANO MIRROR

In this section we consider a system of a waveguide with two side-coupled cavities as in Fig. 1 in the main text, and apply temporal coupled-mode theory [22,26] to calculate the reflection spectrum of the effective mirror. The temporal coupled-mode equations describe the slowly varying envelopes $a_1(t)$ and $a_2(t)$ of the modes of the individual cavities.

The governing equations are

$$\frac{d}{dt} \underline{a}(t) = -i(\underline{\Omega} - \underline{I}\omega_r) \underline{a}(t) + \underline{d}A_+(t), \quad (\text{A1})$$

$$A_-(t) = \underline{d}^T \underline{a}(t), \quad (\text{A2})$$

where $\underline{a} = (a_1, a_2)^T$, $A_+(t)$ and $A_-(t)$ are the incoming and outgoing fields, ω_r is a reference frequency, $\underline{d} = (d_1, d_2)^T = (\sqrt{\gamma_{c1}} e^{i\phi_{1L}}, \sqrt{\gamma_{c2}} e^{i\phi_{2L} + i\theta})^T$ is the vector of coupling constants between waveguide and cavities, and $\underline{\Omega}$ is the system matrix given by

$$\begin{aligned} \underline{\Omega} &= \begin{pmatrix} \omega_{c1} - i\gamma_{c1} - i\gamma_{i1} & \mu + i\sqrt{\gamma_{c1}\gamma_{c2}} e^{i\phi_w} \\ \mu + i\sqrt{\gamma_{c1}\gamma_{c2}} e^{i\phi_w} & \omega_{c2} - i\gamma_{c2} - i\gamma_{i2} \end{pmatrix} \\ &= \begin{pmatrix} \tilde{\omega}_{c1} & \tilde{\mu} \\ \tilde{\mu} & \tilde{\omega}_{c2} \end{pmatrix}. \end{aligned} \quad (\text{A3})$$

Here, $\omega_{c1,2}$ are resonance frequencies of the bare cavities, $\gamma_{c1,2}$ are decay rates related to coupling to the waveguide, $\gamma_{i1,2}$ are decay rates related to intrinsic losses (e.g., vertical scattering), and μ is an evanescent coupling rate assumed real.

Transforming (A1) into the frequency domain, using the definition $e^{-i(\omega - \omega_r)t}$, gives the following solution:

$$\underline{a}(\omega) = [i(\underline{\Omega} - \underline{I}\omega)]^{-1} \underline{d}A_+(\omega), \quad (\text{A4})$$

and the effective reflectivity $r_R(\omega)$ becomes

$$r_R(\omega) = \underline{d}^T [i(\underline{\Omega} - \underline{I}\omega)]^{-1} \underline{d}. \quad (\text{A5})$$

As long as the eigenvalues of $\underline{\Omega}$ are nondegenerate, $r_R(\omega)$ can be expanded as

$$r_R(\omega) = \frac{d_+^2}{i(\omega_+ - \omega) + \gamma_+} + \frac{d_-^2}{i(\omega_- - \omega) + \gamma_-}, \quad (\text{A6})$$

where $\omega_{\pm} - i\gamma_{\pm}$ are the eigenvalues of $\underline{\Omega}$. The coefficients d_{\pm}^2 can be written as

$$d_{\pm}^2 = \frac{1}{2}(d_1^2 + d_2^2) \pm \frac{1}{2} \frac{(\tilde{\Delta}/2)^2 (d_1^2 - d_2^2) + 2\tilde{\mu}d_1d_2}{\sqrt{(\tilde{\Delta}/2)^2 + \tilde{\mu}^2}}, \quad (\text{A7})$$

where $\tilde{\Delta} = \tilde{\omega}_{c2} - \tilde{\omega}_{c1}$. In the case of $\tilde{\Delta} = 0$, we have $d_{\pm}^2 = \frac{1}{2}(d_1 \pm d_2)^2$.

APPENDIX B: STABILITY ANALYSIS

In this section, we derive the characteristic equation (24), starting from Eqs. (16)–(20) in the main text. For simplicity, we assume that the contribution of spontaneous emission into the lasing mode is negligible, such that the exact CW solutions correspond to the solutions of the oscillation condition $r_R(\omega_s)r_L(\omega_s, N_s) = 1$. The Langevin-noise term $F(t)$ can then

be treated as a driving term in the linearized equations. The CW solutions are then given by

$$A(t) = A_s e^{-i(\omega_s - \omega_r)t}, \quad (\text{B1})$$

$$A_-(t) = r_R(\omega_s) A_s e^{-i(\omega_s - \omega_r)t}, \quad (\text{B2})$$

$$N(t) = N_s. \quad (\text{B3})$$

Setting $\frac{d}{dt}N(t) = 0$ gives a relation between N_s and A_s ,

$$R_p - \frac{N_s}{\tau_s} - v_g g(N_s) |A_s|^2 = 0, \quad (\text{B4})$$

where, without loss of generality, A_s can be taken as real.

We now linearize the system around a particular steady-state solution,

$$A(t) = [A_s + \delta A(t)] e^{-i(\omega_s - \omega_r)t}, \quad (\text{B5})$$

$$A_-(t) = [r_R(\omega_s) A_s + \delta A_-(t)] e^{-i(\omega_s - \omega_r)t}, \quad (\text{B6})$$

$$N(t) = N_s + \delta N(t). \quad (\text{B7})$$

Inserting in the dynamical equations (16)–(20), and keeping only terms linear in δ , we get the linearized system

$$\begin{aligned} \delta A(t) &= \frac{1}{2}(1 - i\alpha)\Gamma v_g g_N A_s \tau_L \langle \delta N(t) \rangle A_s \\ &+ \frac{\delta A_-(t - \tau_L)}{r_R(\omega_s)} + F(t), \end{aligned} \quad (\text{B8})$$

$$\begin{aligned} \frac{d}{dt}\delta N(t) &= -\left(\frac{1}{\tau_s} + v_g g_N |A_s|^2\right) \delta N(t) \\ &- v_g g_{th} A_s [\delta A(t) + \delta A^*(t)] + F_N(t), \end{aligned} \quad (\text{B9})$$

where the brackets in $\langle \delta N(t) \rangle$ denote the same time average as in Eq. (17) in the main text. We also added a potential driving term $F_N(t)$ in the carrier density equation.

In the complex frequency domain, the equations become

$$-X(\Omega)\delta A(\Omega) = (1 - i\alpha)\gamma_{AN}O(\Omega)\delta N(\Omega) + F(\Omega), \quad (\text{B10})$$

$$\begin{aligned} -i\Omega\delta N(\Omega) &= -\gamma_R\delta N(\Omega) - \frac{1}{2}\gamma_{NA}[\delta A(\Omega) + \delta A^*(-\Omega^*)] \\ &+ F_N(\Omega), \end{aligned} \quad (\text{B11})$$

where $\gamma_R = \frac{1}{\tau_s} + v_g g_N |A_s|^2$, $\gamma_{AN} = \frac{1}{2}\Gamma v_g g_N A_s$, $\gamma_{NA} = 2v_g g_{th} A_s$, and

$$X(\Omega) = \frac{r_R(\omega_s + \Omega)}{r_R(\omega_s)} e^{i\Omega\tau_L} - 1, \quad O(\Omega) = \frac{e^{i\Omega\tau_L} - 1}{i\Omega}. \quad (\text{B12})$$

A third equation for $\delta A^*(-\Omega^*)$ is obtained by replacing Ω with $-\Omega^*$ in Eq. (B10) and then taking the complex conjugate. Letting an overline denote the combined operation $\overline{f(\Omega)} = f^*(-\Omega^*)$, and then omitting the arguments, the equations are put on matrix form

$$\begin{pmatrix} -X & 0 & -\gamma_{AN}(1 - i\alpha)O \\ 0 & -\overline{X} & -\gamma_{AN}(1 + i\alpha)O \\ \frac{1}{2}\gamma_{NA} & \frac{1}{2}\gamma_{NA} & -i\Omega + \gamma_R \end{pmatrix} \begin{pmatrix} \delta A \\ \overline{\delta A} \\ \delta N \end{pmatrix} = \begin{pmatrix} F \\ \overline{F} \\ F_N \end{pmatrix}. \quad (\text{B13})$$

Taking the determinant of the matrix yields

$$D(\Omega) = X\overline{X}(-i\Omega + \gamma_R) - \frac{1}{2}\omega_R^2 O[X(1 + i\alpha) + \overline{X}(1 - i\alpha)], \quad (\text{B14})$$

where $\omega_R^2 = \gamma_{AN}\gamma_{NA}$. The zeros of the system determinant give the eigenvalues. The real part gives the oscillation frequency of the perturbation, and the imaginary part gives the growth rate, which is negative if the perturbation is damped. Note that since $X(0) = \overline{X}(0) = 0$, then $\Omega = 0$ is always an eigenvalue. The fact that it is *always* an eigenvalue represents the fact that the system is invariant with respect to a global phase.

Finally, for $X, \overline{X} \neq 0$, which is the typical case above threshold $R_p > N_s/\tau_s$, we multiply the determinant with $-i\Omega/\overline{X}$ and arrive at the characteristic equation (22) in the main text,

$$-\Omega^2 - i\gamma_R\Omega + \frac{1}{2}\omega_R^2(H + \overline{H}) = 0, \quad (\text{B15})$$

$$H(\Omega) = (1 - i\alpha) \frac{e^{i\Omega\tau_L} - 1}{\frac{r_R(\omega_s + \Omega)}{r_R(\omega_s)} e^{i\Omega\tau_L} - 1}. \quad (\text{B16})$$

The characteristic equation is now cast in a form that resembles the usual case for a Fabry-Perot laser [47].

-
- [1] H. Hu and L. K. Oxenløwe, Chip-based optical frequency combs for high-capacity optical communications, *Nanophotonics* **10**, 1367 (2021).
- [2] T. Udem, R. Holzwarth, and T. W. Hänsch, Optical frequency metrology, *Nature (London)* **416**, 233 (2002).
- [3] U. Feiste, D. As, and A. Ehrhardt, 18 GHz all-optical frequency locking and clock recovery using a self-pulsating two-section DFB-laser, *IEEE Photonics Technol. Lett.* **6**, 106 (1994).
- [4] M.-G. Suh, Q.-F. Yang, K. Y. Yang, X. Yi, and K. J. Vahala, Microresonator soliton dual-comb spectroscopy, *Science* **354**, 600 (2016).
- [5] V. A. Pammi, K. Alfaro-Bittner, M. G. Clerc, and S. Barbay, Photonic computing with single and coupled spiking micropillar lasers, *IEEE J. Sel. Top. Quantum Electron.* **26**, 1 (2020).
- [6] B. J. Shastri, A. N. Tait, T. Ferreira de Lima, W. H. P. Pernice, H. Bhaskaran, C. D. Wright, and P. R. Prucnal, Photonics for artificial intelligence and neuromorphic computing, *Nat. Photonics* **15**, 102 (2021).
- [7] D. A. B. Miller, Attojoule optoelectronics for low-energy information processing and communications, *J. Lightwave Technol.* **35**, 346 (2017).
- [8] Y. Yu, W. Xue, E. Semenova, K. Yvind, and J. Mork, Demonstration of a self-pulsing photonic crystal Fano laser, *Nat. Photonics* **11**, 81 (2017).
- [9] M. Delmulle, A. Bazin, L. M. Massaro, I. Sagnes, K. Pantzas, S. Combrié, F. Raineri, and A. De Rossi, Self-Pulsing Nanobeam Photonic Crystal Laser, in *Conference on Lasers and Electro-Optics* (Optica Publishing Group, San Jose, California, 2022), p. JW3B.23.
- [10] V. Tronciu, M. Yamada, T. Ohno, S. Ito, T. Kawakami, and M. Taneya, Self-pulsation in an InGaN laser-theory and experiment, *IEEE J. Quantum Electron.* **39**, 1509 (2003).

- [11] H. Wenzel, U. Bandelow, H.-J. Wunsche, and J. Rehberg, Mechanisms of fast self pulsations in two-section DFB lasers, *IEEE J. Quantum Electron.* **32**, 69 (1996).
- [12] C. Rimoldi, L. L. Columbo, J. Bovington, S. Romero-García, and M. Gioannini, Damping of relaxation oscillations, photon-photon resonance, and tolerance to external optical feedback of III-V/SiN hybrid lasers with a dispersive narrow band mirror, *Opt. Express* **30**, 11090 (2022).
- [13] L. Ramunno and J. E. Sipe, Stability of a semiconductor laser with a dispersive extended cavity, *Phys. Rev. A* **66**, 033817 (2002).
- [14] J. Mak, A. van Rees, Y. Fan, E. J. Klein, D. Geskus, P. J. M. van der Slot, and K.-J. Boller, Linewidth narrowing via low-loss dielectric waveguide feedback circuits in hybrid integrated frequency comb lasers, *Opt. Express* **27**, 13307 (2019).
- [15] U. Bandelow, M. Radziunas, V. Z. Tronciu, H.-J. Wunsche, and F. Henneberger, "Tailoring the Dynamics of Diode Lasers by Passive Dispersive Reflectors," *Proc. SPIE 3944, Physics and Simulation of Optoelectronic Devices VIII* (San Jose, CA, 2000), p. 536.
- [16] Y. Yu, A. R. Zali, and J. Mørk, Theory of linewidth narrowing in Fano lasers, *Phys. Rev. Res.* **4**, 043194 (2022).
- [17] J. Mork, Y. Chen, and M. Heuck, Photonic crystal Fano laser: Terahertz modulation and ultrashort pulse generation, *Phys. Rev. Lett.* **113**, 163901 (2014).
- [18] J. Mork, Y. Yu, T. S. Rasmussen, E. Semenova, and K. Yvind, Semiconductor Fano lasers, *IEEE J. Sel. Top. Quantum Electron.* **25**, 1 (2019).
- [19] U. Fano, Effects of configuration interaction on intensities and phase shifts, *Phys. Rev.* **124**, 1866 (1961).
- [20] S. Matsuo, A. Shinya, T. Kakitsuka, K. Nozaki, T. Segawa, T. Sato, Y. Kawaguchi, and M. Notomi, High-speed ultracompact buried heterostructure photonic-crystal laser with 13 fJ of energy consumed per bit transmitted, *Nat. Photonics* **4**, 648 (2010).
- [21] Y. Yu, A. Sakanas, A. R. Zali, E. Semenova, K. Yvind, and J. Mørk, Ultra-coherent Fano laser based on a bound state in the continuum, *Nat. Photonics* **15**, 758 (2021).
- [22] S. Fan, W. Suh, and J. D. Joannopoulos, Temporal coupled-mode theory for the Fano resonance in optical resonators, *J. Opt. Soc. Am. A* **20**, 569 (2003).
- [23] T. S. Rasmussen, Y. Yu, and J. Mork, Suppression of coherence collapse in semiconductor Fano lasers, *Phys. Rev. Lett.* **123**, 233904 (2019).
- [24] G. Dong, S. L. Liang, A. Sakanas, E. Semenova, K. Yvind, J. Mørk, and Y. Yu, Cavity dumping using a microscopic Fano laser, *Optica* **10**, 248 (2023).
- [25] D. Bekele, Y. Yu, K. Yvind, and J. Mork, In-plane photonic crystal devices using Fano resonances, *Laser Photonics Rev.* **13**, 1900054 (2019).
- [26] W. Suh, Z. Wang, and S. Fan, Temporal coupled-mode theory and the presence of non-orthogonal modes in lossless multimode cavities, *IEEE J. Quantum Electron.* **40**, 1511 (2004).
- [27] Y. Yan, Y.-F. Jiang, B.-X. Li, and C.-S. Deng, Controlling dual Fano resonance lineshapes based on an indirectly coupled double-nanobeam-cavity photonic molecule, *J. Lightwave Technol.* **42**, 732 (2023).
- [28] M. Heuck, P. T. Kristensen, and J. Mørk, Dual-resonances approach to broadband cavity-assisted optical signal processing beyond the carrier relaxation rate, *Opt. Lett.* **39**, 3189 (2014).
- [29] M. Saldutti, M. Xiong, E. Dimopoulos, Y. Yu, M. Gioannini, and J. Mørk, Modal properties of photonic crystal cavities and applications to lasers, *Nanomaterials* **11**, 3030 (2021).
- [30] G. Dong, M. Xiong, E. Dimopoulos, A. Sakanas, E. Semenova, K. Yvind, Y. Yu, and J. Mørk, Experimental demonstration of a nanobeam Fano laser, *Opt. Express* **32**, 5242 (2024).
- [31] A. R. A. Chalcraft, S. Lam, B. D. Jones, D. Szymanski, R. Oulton, A. C. T. Thijssen, M. S. Skolnick, D. M. Whittaker, T. F. Krauss, and A. M. Fox, Mode structure of coupled L3 photonic crystal cavities, *Opt. Express* **19**, 5670 (2011).
- [32] C. W. Hsu, B. Zhen, A. D. Stone, J. D. Joannopoulos, and M. Soljačić, Bound states in the continuum, *Nat. Rev. Mater.* **1**, 16048 (2016).
- [33] P. T. Kristensen, J. R. de Lasson, M. Heuck, N. Gregersen, and J. Mork, On the theory of coupled modes in optical cavity-waveguide structures, *J. Lightwave Technol.* **35**, 4247 (2017).
- [34] S. Haddadi, P. Hamel, G. Beaudoin, I. Sagnes, C. Sauvan, P. Lalanne, J. A. Levenson, and A. M. Yacomotti, Photonic molecules: tailoring the coupling strength and sign, *Opt. Express* **22**, 12359 (2014).
- [35] Y. Yu, E. Palushani, M. Heuck, N. Kuznetsova, P. T. Kristensen, S. Ek, D. Vukovic, C. Peucheret, L. K. Oxenløwe, S. Combrié, A. de Rossi, K. Yvind, and J. Mørk, Switching characteristics of an InP photonic crystal nanocavity: Experiment and theory, *Opt. Express* **21**, 31047 (2013).
- [36] E. Detoma, B. Tromborg, and I. Montrosset, The complex way to laser diode spectra: example of an external cavity laser strong optical feedback, *IEEE J. Quantum Electron.* **41**, 171 (2005).
- [37] U. Feiste, Optimization of modulation bandwidth in DBR lasers with detuned Bragg reflectors, *IEEE J. Quantum Electron.* **34**, 2371 (1998).
- [38] J. Piprek, *Optoelectronic Devices: Advanced Simulation and Analysis* (Springer, New York, 2005).
- [39] M. Chacinski and R. Schatz, Impact of losses in the Bragg section on the dynamics of detuned loaded DBR lasers, *IEEE J. Quantum Electron.* **46**, 1360 (2010).
- [40] B. Tromborg, J. Mørk, and V. Velichansky, On mode coupling and low-frequency fluctuations in external-cavity laser diodes, *Quantum Semiclassical Opt.* **9**, 831 (1997).
- [41] C. Rimoldi, L. L. Columbo, J. Bovington, S. Romero-Garcia, and M. Gioannini, CW emission and self-pulsing in a III-V/SiN hybrid laser with narrow band mirror, *IEEE Photonics J.* **14**, 1 (2022).
- [42] A. Bogatov, P. Eliseev, and B. Sverdlov, Anomalous interaction of spectral modes in a semiconductor laser, *IEEE J. Quantum Electron.* **11**, 510 (1975).
- [43] M. Marconi, J. Javaloyes, F. Raineri, J. A. Levenson, and A. M. Yacomotti, Asymmetric mode scattering in strongly coupled photonic crystal nanolasers, *Opt. Lett.* **41**, 5628 (2016).
- [44] V. Tronciu, N. Werner, H. Wenzel, and H.-J. Wunsche, Feedback sensitivity of detuned DBR semiconductor lasers, *IEEE J. Quantum Electron.* **57**, 1 (2021).
- [45] K. Vahala and A. Yariv, Detuned loading in coupled cavity semiconductor lasers—effect on quantum noise and dynamics, *Appl. Phys. Lett.* **45**, 501 (1984).
- [46] B. Tromborg, H. Olesen, Xing Pan, and S. Saito, Transmission line description of optical feedback and injection locking for Fabry-Perot and DFB lasers, *IEEE J. Quantum Electron.* **23**, 1875 (1987).

- [47] L. A. Coldren, S. W. Corzine, and M. L. Mašanović, *Diode Lasers and Photonic Integrated Circuits: Coldren/Diode Lasers 2E* (Wiley, Hoboken, 2012).
- [48] T. S. Rasmussen, Y. Yu, and J. Mork, Modes, stability, and small-signal response of photonic crystal Fano lasers, *Opt. Express* **26**, 16365 (2018).
- [49] G. P. Agrawal and N. K. Dutta, *Semiconductor Lasers* (Springer, Boston, 1993).
- [50] H. J. Wünsche, O. Brox, M. Radziunas, and F. Henneberger, Excitability of a semiconductor laser by a two-mode homoclinic bifurcation, *Phys. Rev. Lett.* **88**, 023901 (2001).
- [51] Y.-C. Liu, B.-B. Li, and Y.-F. Xiao, Electromagnetically induced transparency in optical microcavities, *Nanophotonics* **6**, 789 (2017).
- [52] P. Hamel, S. Haddadi, F. Raineri, P. Monnier, G. Beaudoin, I. Sagnes, A. Levenson, and A. M. Yacomotti, Spontaneous mirror-symmetry breaking in coupled photonic-crystal nanolasers, *Nat. Photonics* **9**, 311 (2015).
- [53] M. Marconi, F. Raineri, A. Levenson, A. M. Yacomotti, J. Javaloyes, S. H. Pan, A. E. Amili, and Y. Fainman, Mesoscopic limit cycles in coupled nanolasers, *Phys. Rev. Lett.* **124**, 213602 (2020).
- [54] D. Huang, M. A. Tran, J. Guo, J. Peters, T. Komljenovic, A. Malik, P. A. Morton, and J. E. Bowers, High-power sub-kHz linewidth lasers fully integrated on silicon, *Optica* **6**, 745 (2019).
- [55] J.-C. Li, Y.-T. Huang, C.-G. Ma, Z.-N. Zhang, J.-L. Xiao, Y.-D. Yang, and Y.-Z. Huang, Self-pulsing and dual-mode lasing in a square microcavity semiconductor laser, *Opt. Lett.* **48**, 4953 (2023).